

Signatures of Mottness and Hundness in archetypal correlated metals

Xiaoyu Deng,^{1,*} Katharina M. Stadler,^{2,*} Kristjan Haule,¹
 Andreas Weichselbaum,^{3,2} Jan von Delft,² and Gabriel Kotliar^{1,3}

¹*Department of Physics and Astronomy, Rutgers University, Piscataway, New Jersey 08854, USA*

²*Physics Department, Arnold Sommerfeld Center for Theoretical Physics and Center for NanoScience,
 Ludwig-Maximilians-Universität München, 80333 München, Germany*

³*Condensed Matter Physics and Materials Science Department,
 Brookhaven National Laboratory, Upton, New York 11973, USA*

(Dated: March 7, 2024)

Physical properties of multi-orbital materials depend not only on the strength of the effective interactions among the valence electrons but also on their type. Strong correlations are caused by either Mott physics that captures the Coulomb repulsion among charges, or Hund physics that aligns the spins in different orbitals. We identify four energy scales marking the onset and the completion of screening in orbital and spin channels. The differences in these scales, which are manifest in the temperature dependence of the local spectrum and of the charge, spin and orbital susceptibilities, provide clear signatures distinguishing Mott and Hund physics. We illustrate these concepts with realistic studies of two archetypal strongly correlated materials, and corroborate the generality of our conclusions with a model Hamiltonian study.

The excitation spectra and transport properties of transition metal oxides at high energy and/or high temperature are well described in terms of dressed atomic excitations with their characteristic multiplet structure. At very low energy scales, by contrast, metallic systems are well described in terms of strongly renormalized Landau quasiparticles forming dispersive bands. Describing the evolution of the excitation spectrum as a function of energy scale is a fundamental problem in the theory of strongly correlated materials. Starting with the Fermi liquid quasiparticles at the lowest energy scales, and raising the temperature, one can view this evolution as their gradual undressing. Conversely, starting from the high energy end, one can understand the evolution of the excitation spectrum as the screening of the orbital and spin excitations of atomic states, which gradually bind to give rise to quasiparticles. Here we consider the temperature dependence of this screening process for correlated multi-orbital systems with strong on-site atomic-like interactions, involving both a Coulomb repulsion U and Hund's coupling J . The former differentiates between different charge configurations without preference for a given spin or orbital configuration, whereas the latter favors the highest spin state.

It is well known that strong correlation effects can arise due to proximate Mott insulating states in which strong on-site Coulomb repulsion slows down charge fluctuations or even blocks the charge motion and localizes the electrons [1, 2]. However, many materials far away from the Mott insulating state, notably the 3d iron-based superconductors [3, 4] and ruthenates [5, 6], display strong correlation effects as a result of strong Hund coupling rather than the Hubbard U . These so-called “Hund metals” [3–14] were proposed to be a new type of strongly correlated electron system, characterized by spin-orbital separation [9–11].

The existence of different origins of correlations, Coulomb U or Hund J , poses an important questions: what are the defining signatures distinguishing Mott and Hund metals? The goal of this work is to answer this question, by pointing out that Hund and Mott metals differ strikingly in the temperature dependencies of their local correlated spectra and the local susceptibilities describing the charge, spin and orbital degrees of freedom. These differences reflect two distinct screening routes for how quasiparticles emerge from the atomic degrees of freedom, with spin-orbital separation involved for Hund metals, but not for Mott metals.

We provide evidence of the two distinct screening routes by investigating (i) two realistic materials and (ii) a model Hamiltonian. For (i) we consider two archetypal materials with non-degenerate orbitals, the Mott system V_2O_3 [15–17] and the Hund metal Sr_2RuO_4 [18]. We compute their properties using density functional theory plus dynamical mean-field theory (DFT+DMFT) [19–21], which has been successfully used to describe the available experimental measurements for V_2O_3 [22–28] and Sr_2RuO_4 [5, 29–31]. For (ii) we study a 3-band Hubbard-Hund model (3HHM) with three degenerate bands hosting two electrons. This 3HHM is the simplest model capable of capturing both Hund and Mott physics and the crossover between them as function of increasing U [9, 10]. Whereas Ref. [10] focused on $T = 0$, here we focus on temperature dependence. We study the 3HHM using DMFT and the numerical renormalization group (DMFT+NRG). We accurately determine the location of the Mott transition at zero temperature and show that provided that J is sizeable, the temperature dependence of physical properties for large U near the Mott transition line qualitatively resembles that of V_2O_3 , while for small U far from the transition it

* These authors contributed equally to this work. Correspondence: xiaoyu.deng@gmail.com.

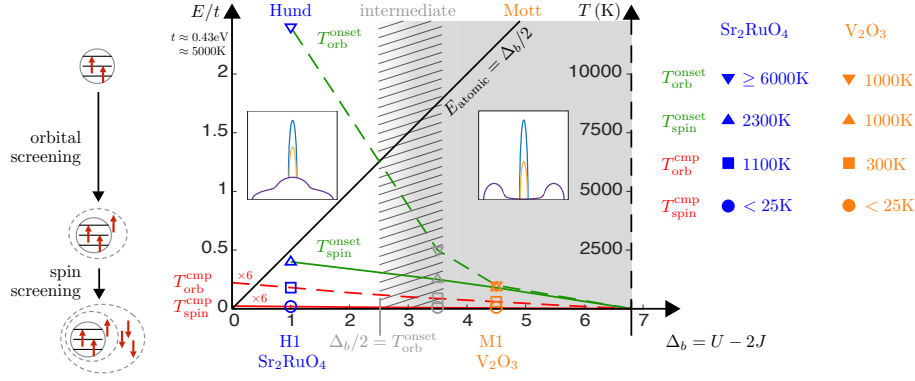


FIG. 1. Schematic sketch of the behavior of four characteristic temperature scales, $T_{\text{orb}}^{\text{onset}}$ (green dashed), $T_{\text{spin}}^{\text{onset}}$ (green solid), $T_{\text{orb}}^{\text{cmp}}$ (red dashed), $T_{\text{spin}}^{\text{cmp}}$ (red solid), marking the onset and the completion of screening of orbital and spin degrees of freedom, respectively, as functions of the bare gap, $\Delta_b = U - 2J$, between the upper and lower Hubbard side band. Open symbols on the left give the values of these scales as obtained from DMFT+NRG calculations for our 3-band Hubbard-Hund model, with $J = 1$ and $U = 3$ (green), $U = 5.5$ (grey) and $U = 6.5$ (yellow). On the right, closed symbols give corresponding values obtained from DFT+DMFT calculations for the materials Sr_2RuO_4 (green) and V_2O_3 (yellow). Left: cartoon of two-stage screening for three local levels with $J \neq 0$, containing two electrons with total spin $S = 1$: with decreasing temperature, first orbital screening of the hole occurs, whereby a delocalized spin 1/2 combines with the local spin 1 to yield an orbital singlet with spin 3/2; then spin screening occurs, yielding an orbital and spin singlet [10]. The energy scales characterizing the two screening stages lie far apart for Hund systems, but close together for Mott systems. Insets: cartoons of the local density of states, $A(\omega)$, for a Hund system (left) and a Mott system close to the Mott transition (right), summarizing the essential differences in the evolution of the quasiparticle peak with decreasing temperature (purple to yellow to blue).

resembles that of Sr_2RuO_4 . Therefore, our 3HHM results elucidate the physical origin of the differences between these materials. Indeed, we argue that our findings are applicable to general multi-orbital materials and characteristic of the general phenomenology of Mott and Hund physics, independent of material-dependent details, such as the initial band structure.

Overview of results

We start with an overview of our most important observations. We first identify four temperature scales, characterizing the onset and completion of screening of the orbital and spin degrees of freedom as the temperature is lowered. The scales for the onset of screening, $T_{\text{orb}}^{\text{onset}}$ and $T_{\text{spin}}^{\text{onset}}$, are defined as the temperatures at which the static local orbital and spin susceptibilities, χ_{orb} and χ_{spin} , first show deviations from the Curie behavior, $\chi \propto 1/T$, shown by free local moments. The scales for the completion of screening, $T_{\text{orb}}^{\text{cmp}}$ and $T_{\text{spin}}^{\text{cmp}}$, mark the transition of these susceptibilities to Pauli behavior, saturating to constants at very low temperatures. For orientation, Fig. 1 summarizes the behavior of these scales with increasing Coulomb interaction at fixed Hund's coupling, as will be elaborated throughout the text below. The most striking observation is that increasing U pushes the onset scales $T_{\text{orb}}^{\text{onset}}$ and $T_{\text{spin}}^{\text{onset}}$ closer together until they essentially coincide. As a consequence, the Hund regime (small U) and the Mott regime (large U , close to the Mott transition), though adiabatically connected via a crossover regime, show dramatic differences for the temperature dependence of physical quantities (discussed below). The trends shown in the figure were extracted from our analysis of the 3HHM, but they match those found for V_2O_3 and Sr_2RuO_4 (see legend on the right), and we expect them to be generic for multi-orbital Mott and/or Hund systems.

Mott systems. Coulomb interactions are strong in Mott systems, so that there is a large separation between the upper and lower Hubbard bands associated with atomic excitations, resulting in a significant gap or pseudogap. It is well established that, in the context of a metal-insulator transition, a metallic state is induced by the formation of a quasiparticle resonance from either the center of the gap or the edges of the Hubbard bands. Vice versa, starting from a correlated metal of Mott-type, a gap (or pseudogap) between incoherent spectra is restored when the coherence resonance is destroyed. The transition from insulator to metal can be induced by doping or tuning the ratio of the interaction versus the bandwidth [2], but it also occurs when the coherence resonance emerges by decreasing temperature. For example, in a model study of a doped single-band Mott insulator at infinite dimensions, the spectra at high temperature exhibit a two-peak structure reminiscent of a Mott gap, from which a coherence resonance emerges as “resilient quasiparticles” appear [45].

Here we propose that the presence of a gap/pseudogap regime in the local density of states (LDOS) at temperatures so high that the coherence resonance is destroyed is a fingerprint of Mott physics in general situations. We show that, at high temperatures, the LDOS of a multi-orbital Mott system exhibits two incoherent peaks above and below

the Fermi energy, reflecting atomic particle- and hole-like excitations, with a pseudogap in between, signifying the proximity to charge localization. When the temperature is lowered, a clear and sharp quasiparticle resonance suddenly emerges near the Fermi energy (for a cartoon depiction, see Fig. 1, right inset), signifying the appearance of mobile charge carriers. This occurs at a well-defined temperature scale, T_M , well below the lowest atomic excitation energy, E_{atomic} , involved in the incoherent two-peak structure. This Mott behavior is also reflected in the temperature dependence of various local susceptibilities. With decreasing temperature the static local charge susceptibility and local charge fluctuations first remain small and rather constant while the local spin and orbital susceptibilities exhibit Curie behavior, indicative of unscreened local moments. Once the temperature drops below T_M , the appearance of mobile carriers causes the local charge susceptibility and charge fluctuations to increase, and the spin and orbital susceptibilities to deviate from pure Curie behavior, reflecting the onset of screening. For Mott systems, this onset thus occurs simultaneously for orbital and spin degrees of freedom, $T_{\text{spin}}^{\text{onset}} = T_{\text{orb}}^{\text{onset}} = T_M$.

Hund systems. The above signatures of Mott physics are in stark contrast to the behavior of Hund systems. These typically have much smaller values of U , and hence E_{atomic} . Consequently, the Hubbard side bands effectively overlap, so that the LDOS features a single incoherent peak even at temperatures as high as E_{atomic} or beyond. This broad peak evolves into a coherent quasiparticle peak as the temperature is lowered (for a cartoon depiction, see Fig. 1, left inset). Due to the absence of a pseudogap at large temperatures, the local charge susceptibility is large already at high temperatures and increases continuously, but only slightly, with decreasing temperature. Strikingly, the local orbital and spin susceptibilities show deviations from Curie-like behavior already at much higher temperatures than those in Mott systems. Moreover, orbital screening starts well before spin screening, $T_{\text{orb}}^{\text{onset}} \gg T_{\text{spin}}^{\text{onset}}$. Thus, Hund metals exhibit spin-orbital separation, featuring a broad temperature window, from $T_{\text{orb}}^{\text{onset}}$ down to $T_{\text{spin}}^{\text{onset}}$, involving screened, delocalized orbitals coupled to unscreened, localized spins. Importantly, $T_{\text{orb}}^{\text{onset}}$ can be much larger than E_{atomic} in Hund metals, which is why no pseudogap appears even up to temperatures well above E_{atomic} (it would appear only for $T \gtrsim T_{\text{orb}}^{\text{onset}}$, since it requires the breakdown of both spin *and* orbital screening). The fact that $T_{\text{spin}}^{\text{onset}}$ and E_{atomic} are both $\ll T_{\text{orb}}^{\text{onset}}$ is a crucial difference relative to Mott systems. There $T_{\text{spin}}^{\text{onset}} \simeq T_{\text{orb}}^{\text{onset}} \ll E_{\text{atomic}}$, so that the breakdown of spin and orbital screening, and the concomitant emergence of a pseudogap, is possible at temperatures well below E_{atomic} .

In principle, both multi-orbital Mott and Hund materials exhibit spin-orbital separation in the *completion* of screening: χ_{orb} crosses over to Pauli behavior at a larger temperature scale than χ_{spin} , i.e. $T_{\text{orb}}^{\text{cmp}} \gg T_{\text{spin}}^{\text{cmp}}$. Since Fermi-liquid behavior occurs below $T_{\text{spin}}^{\text{cmp}}$, this scale can be identified with the Fermi-liquid scale $T_{\text{FL}} \equiv T_{\text{spin}}^{\text{cmp}}$. However, spin-orbital separation in the completion of screening is much more pronounced for the Hund material.

Two archetypical materials: V_2O_3 and Sr_2RuO_4

Established facts. We begin our discussion of the two example materials by summarizing some of their well-established properties. V_2O_3 , a paramagnetic metal at ambient conditions, is proximate to an isostructural Mott transition (that can be induced by slightly Cr-doping), and a temperature-driven magnetic transition [15–17]. It exhibits Fermi-liquid behavior at low temperature when antiferromagnetism is quenched by doping or pressure [15–17]. Sr_2RuO_4 , on the other hand, is a paramagnetic metal far away from a Mott insulating state [33]. As temperature decreases it shows Fermi-liquid behavior and eventually becomes superconducting at very low temperature [18]. Despite the very different distances to a Mott insulating state, both materials have large specific heat coefficients in their Fermi-liquid states [15–18]. In both materials the observed Fermi-liquid scales are extremely low (around 25K [15–17, 34]), much smaller than the bare band energy or interaction parameters (order of eV). Pronounced quasiparticle peaks are observed in both materials using photoemission spectroscopy [35–38], and large values of mass renormalization are seen in Sr_2RuO_4 in various measurements [39–41]. Notably, the local physics on V/Ru sites are similar, with nominally two electrons/holes in three t_{2g} orbitals. Due to the crystal field of the surrounding oxygen, the t_{2g} orbitals of V are split into e_g^π orbitals with two-fold degeneracy and an energetically higher-lying a_{1g} orbital, while those of Ru are split into xz/yz orbitals with two-fold degeneracy and an energetically lower-lying xy orbital. Two electrons (holes) in three orbitals favor a spin-triplet $S = 1$ atomic state because of Hund’s coupling in both V_2O_3 [22, 42–44] and Sr_2RuO_4 [5].

Local spectra.

We compute the spectra of the relevant correlated orbitals in V_2O_3 and Sr_2RuO_4 up to high temperature with DFT+DMFT. We have not taken into account the effects of the temperature-dependent changes in lattice parameters, which have been shown to be very important in materials near the Mott transition such as V_2O_3 [32]. Nevertheless, the LDA+DMFT calculations here bring a degree of realism, such as band structure and crystal field effects, which is not present in the 3HHM calculations discussed further below. We focus first on the density of states at the Fermi level, estimated via $D(i\omega_0) = -\frac{1}{\pi} \text{Im}G(i\omega_0)$ (ω_0 is the first Matsubara frequency, G the computed local Green’s function). Fig. 2(a) depicts the temperature dependence of $D(i\omega_0)$ for e_g^π and a_{1g} orbitals in V_2O_3 . The results show that both orbitals share a characteristic temperature, $T_M = 1000\text{K}$: $D(i\omega_0)$ is fairly flat at temperatures above T_M , which implies approximately “rigid”, i.e. temperature-independent, spectra. Below T_M , $D(i\omega_0)$ gradually acquires

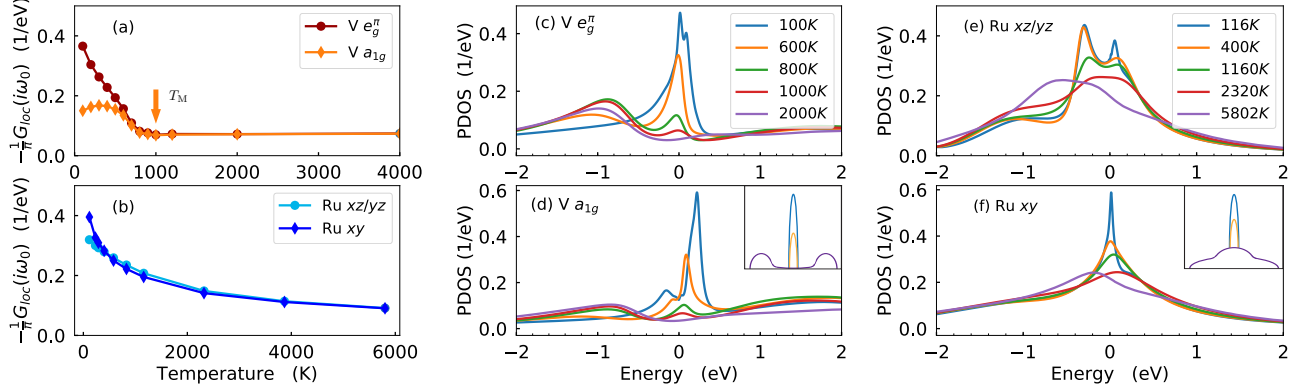


FIG. 2. The local spectra of the correlated orbitals in V_2O_3 [panels (a,c,d)] and Sr_2RuO_4 [panels (b,e,f)] exhibit different behaviors in their temperature dependence. (a,b) The density of states at the Fermi level, estimated by $D(i\omega_0) = -\frac{1}{\pi}\text{Im}G(i\omega_0)$. (c-f) The correlated real-frequency spectra (PDOS), $D(\omega) = -\frac{1}{\pi}\text{Im}G(\omega)$. $D(i\omega_0)$ shows a suppression at a characteristic temperature $T_M = 1000\text{K}$ (indicated by the purple arrow) in V_2O_3 (a), while it evolves smoothly in Sr_2RuO_4 (b). As temperature decreases, in V_2O_3 the coherence resonance of both e_g^π and a_{1g} orbitals emerges from the pseudogap regime with low density of states between two incoherent peaks (c,d), while in Sr_2RuO_4 the coherence resonance of both $d_{xz/yz}$ and d_{xy} orbitals emerges from a single broad incoherent peak with large finite density of states at the Fermi level (e,f). The insets in (d,f), repeated from Fig. 1, are cartoons of the temperature dependence of the Mott and Hund PDOS.

a larger magnitude in both orbitals as temperature is lowered, signaling the formation of a quasiparticle resonance. We note that it increases monotonically with decreasing temperature in the e_g^π orbitals, but in the a_{1g} orbital it first increases and then decreases a little. Thus at low temperature the density of states at the Fermi level has a dominant e_g^π character. We emphasize that the evolution of $D(i\omega_0)$ is smooth and a first-order MIT is not involved. By contrast, in Sr_2RuO_4 the temperature dependence of the densities of states, $D(i\omega_0)$, of $d_{xz/yz}$ and d_{xy} orbitals is very different, as depicted in Fig. 2(b). For both orbitals, $D(i\omega_0)$ increases as temperature is decreased, with gradually increasing slope, showing no flat regime even at extremely high temperatures, where their values are already larger than those for V_2O_3 above T_M . In contrast to the case of V_2O_3 , a quasiparticle resonance is present even at the highest temperatures studied and, thus, no characteristic temperature is found for its onset, as discussed in the next paragraph.

We also study the correlated real-frequency projected density of states (PDOS), $D(\omega) = -\frac{1}{\pi}\text{Im}G(\omega)$, for the different orbitals. These are obtained by analytically continuing the computed Matsubara self-energy and then computing the local Green's function. The results for V_2O_3 are depicted in Fig. 2(c,d). At very high temperatures, we observe a typical Mott feature: a pseudogap exists at the Fermi level, between two broad humps in the incoherent spectra, with maxima near -1eV and 2eV . With decreasing temperature spectral weight is transferred from the high-energy humps into the pseudogap and a quasiparticle peak emerges similarly in both orbitals at the Fermi level on top of the pseudogap. The characteristic temperature for the onset of the formation of the coherence resonance is roughly consistent with $T_M = 1000\text{K}$ determined above. As temperature decreases further, the magnitude of the coherence peak in both orbitals increases gradually, and at very low temperature both orbitals show a coherence resonance with a pronounced, thin cusp. In the e_g^π orbitals the resonance is peaked at the Fermi level while the a_{1g} quasiparticle peak slightly moves away from the Fermi level when the temperature is lowered, thus reducing the density of states at the Fermi level. The resulting temperature evolution of the zero-frequency density of states in both orbitals is consistent with the $D(i\omega_0)$ discussed above, including the non-monotonic behavior of the a_{1g} orbital in Fig. 2(a). For Sr_2RuO_4 the slow increase of the density of states at the Fermi level, $D(i\omega_0)$, with decreasing temperature becomes clear from the PDOS, shown in Fig. 2(e,f). The correlated high-temperature local spectra are characterized by a single broad feature (no side-humps), which shifts its position slightly towards the Fermi level with decreasing temperature, while its shape remains almost unchanged. This is very different from the spectra in V_2O_3 , which at high temperatures show a pseudogap between two broad side peaks. When the temperature is decreased further, a sharp narrow peak gradually develops in both orbitals from the broad, incoherent feature. In this process only a small fraction of spectral weight is transferred from higher frequencies to a 1eV range around the Fermi level. At low temperature, the spectra of both $d_{xz/yz}$ and d_{xy} orbitals are similar to their corresponding DFT values with a renormalized bandwidth and show a pronounced, thin cusp as in the case of V_2O_3 .

The different temperature dependences of the local spectra of V_2O_3 and Sr_2RuO_4 can be viewed as fingerprints distinguishing Mott from Hund systems, respectively. With decreasing temperature the quasiparticle resonance of

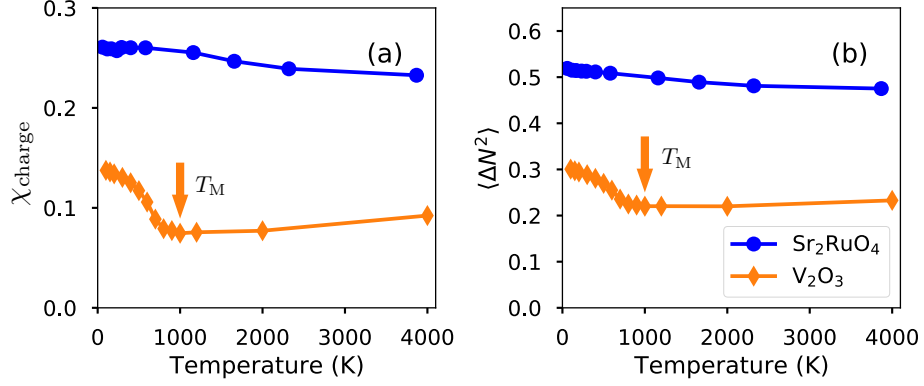


FIG. 3. (a) The static local charge susceptibility χ_{charge} , and (b) local charge fluctuation $\langle \Delta N^2 \rangle$, computed for V_2O_3 (diamonds) and Sr_2RuO_4 (circles). In the Hund system Sr_2RuO_4 both χ_{charge} and $\langle \Delta N^2 \rangle$ are large and only weakly dependent on temperature. By contrast, in the Mott system V_2O_3 they are much smaller and strongly temperature-dependent. The purple arrows indicate that in V_2O_3 the minima of the local charge susceptibility and fluctuation occur at the same temperature scale, T_M , as that marking the emergence of the quasiparticle peak in the local PDOS.

V_2O_3 emerges from a high-temperature pseudogap regime with very low density of states between incoherent spectra [see purple curve in the cartoon in inset of Fig. 2(d)]. This is consistent with the widely held belief that Mott physics governs V_2O_3 . It is described by a single characteristic temperature scale, T_M , which indicates the onset of formation of the quasiparticle resonance. By contrast, for Sr_2RuO_4 the quasiparticle resonance develops with decreasing temperature from a single incoherent peak that has a large value at the Fermi level already at very high temperature [see purple curve in the cartoon in inset of Fig. 2(f)]. The demonstration of these two distinct routes towards forming the coherent Fermi-liquid at low temperature is one of the main results of this work.

Susceptibilities. We next consider the static local charge susceptibility, $\chi_{\text{charge}} = \int_0^\beta \langle N_d(\tau) N_d(0) \rangle d\tau - \beta \langle N_d \rangle^2$, and the local charge fluctuations, $\langle \Delta N^2 \rangle = \langle N_d^2 \rangle - \langle N_d \rangle^2$, shown in Figs. 3(a) and 3(b), respectively. (N_d is the total occupancy of t_{2g} orbitals.) For both materials, the behavior of χ_{charge} mimics that of $\langle \Delta N^2 \rangle$, hence we focus on the latter below. $\langle \Delta N^2 \rangle$ is much smaller, with a much stronger temperature dependence, in V_2O_3 than in Sr_2RuO_4 . For V_2O_3 , $\langle \Delta N^2 \rangle$ initially remains small and almost constant with decreasing temperature, signifying the suppression of charge fluctuations in the pseudogap regime. It then increases rather abruptly, signifying the onset of charge delocalization, at the same temperature, $T_M = 1000\text{K}$ (purple arrow in Fig. 3(a)), as that where the quasiparticle peak begins to emerge. By contrast, for Sr_2RuO_4 $\langle \Delta N^2 \rangle$ exhibits only a weak temperature dependence, persisting up to the highest temperature studied but changing by less than 10% over this range.

We have also computed the static local spin and orbital susceptibilities, defined as $\chi_{\text{spin}} = \int_0^\beta \langle S_z(\tau) S_z(0) \rangle d\tau$ and $\chi_{\text{orb}} = \int_0^\beta \langle \Delta N_{\text{orb}}(\tau) \Delta N_{\text{orb}}(0) \rangle d\tau - \beta \langle \Delta N_{\text{orb}} \rangle^2$, where S_z is the total spin momentum in the t_{2g} orbitals, $\Delta N_{\text{orb}} = N_d/2 - N_b$ is the occupancy difference per orbital, and (a, b) denotes (e_g^{π}, a_{1g}) in V_2O_3 and $(xz/yz, xy)$ in Sr_2RuO_4 , respectively. The results are depicted in Fig. 4. In V_2O_3 , both the spin and orbital susceptibilities exhibit Curie behavior, i.e. $T_{\chi_{\text{spin}}}$ and $T_{\chi_{\text{orb}}}$ are approximately constant at high temperature (Fig. 4(a)). Notably, with decreasing temperature deviations from the Curie behavior set in at the same characteristic temperature, $T_M = 1000\text{K}$, as that determined above from the local PDOS evolution. Thus, spin and orbital degrees of freedom start to be screened simultaneously with the formation of a coherence resonance in the prototype Mott system V_2O_3 , $T_{\text{orb}}^{\text{onset}} = T_{\text{spin}}^{\text{onset}} = T_M$. By contrast, in the Hund material Sr_2RuO_4 , Curie-like behavior in the spin susceptibility is seen only at very high temperatures. With decreasing temperature, it ceases already at around $T_{\text{spin}}^{\text{onset}} \simeq 2300\text{K}$ (Fig. 4(c)), a scale much higher than that in V_2O_3 . For the orbital susceptibility the situation is even more extreme: it does not show Curie behavior even at the highest temperature studied ($T_{\text{orb}}^{\text{onset}} \geq 6000\text{K}$). This is evidence of spin-orbital separation in Sr_2RuO_4 : the screening of the orbital degrees of freedom starts at much higher temperature than that of the spin degrees of freedom, $T_{\text{orb}}^{\text{onset}} \gg T_{\text{spin}}^{\text{onset}}$. Hence the onset of deviations from Curie-like behavior in the spin/orbital susceptibility, i.e. the onset of screening of spin/orbital degrees of freedom, is very different in V_2O_3 and Sr_2RuO_4 . These differences constitute another set of fingerprints distinguishing Mott from Hund systems. It will be further analyzed below in the context of our 3HHM calculations.

Next we discuss the completion of orbital and spin screening, characterized by the temperature scales, $T_{\text{orb}}^{\text{cmp}}$ and $T_{\text{spin}}^{\text{cmp}}$, below which the corresponding susceptibilities become constant. In both materials, χ_{orb} seems to become essentially constant at low temperatures, with the orbital screening completion scale in V_2O_3 , $T_{\text{orb}}^{\text{cmp}} \simeq 300\text{K}$ (Fig. 4(b)),

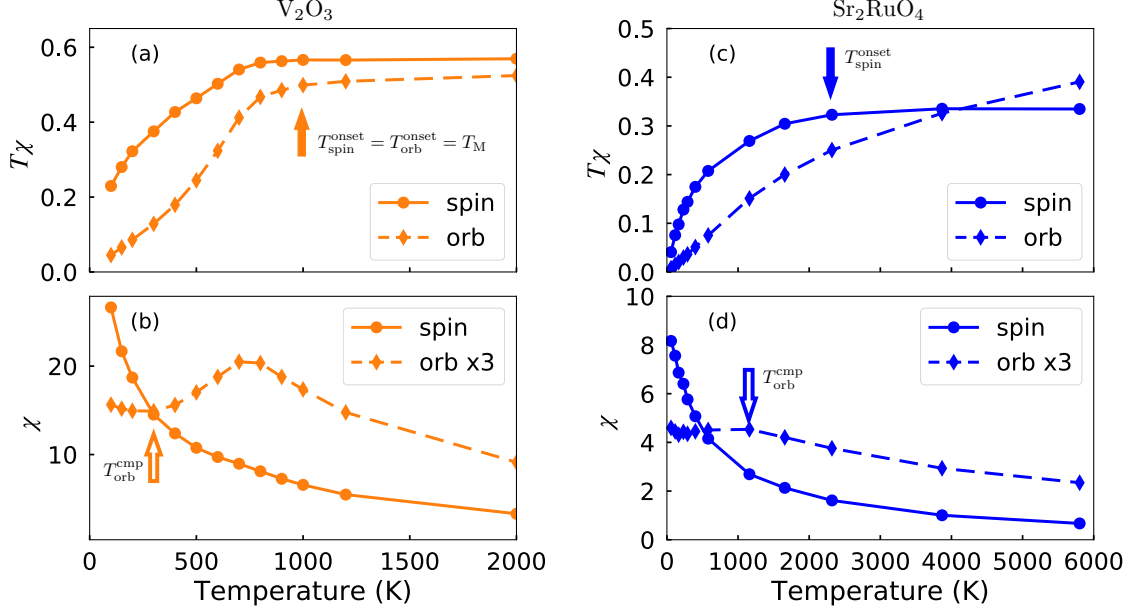


FIG. 4. The static local orbital and spin susceptibilities χ_{orb} and χ_{spin} of V_2O_3 (a,b) and Sr_2RuO_4 (c,d), plotted as functions of temperature, with $T\chi$ and χ shown in the upper and lower panels, respectively. The Curie law holds above 1000K (indicated by open purple arrow) in the spin and orbital susceptibility of V_2O_3 (a). In Sr_2RuO_4 the spin susceptibility follows Curie-like behavior above 2300K (indicated by open cyan arrow), while the orbital susceptibility does not follow a Curie law in the temperature range studied (c). The spin susceptibility of both materials (b,d) does not saturate at the lowest accessible temperature, indicating an even lower Fermi-liquid scale. The orbital susceptibility has only weak temperature dependence below 300K in V_2O_3 (b) and below 1100K in Sr_2RuO_4 (d) (indicated by filled blue arrows).

being much smaller than in Sr_2RuO_4 , $T_{\text{orb}}^{\text{cmp}} \simeq 1100\text{K}$ (Fig. 4(d)). By contrast, in both materials the spin susceptibility increases with decreasing temperature, and is not fully screened even at the lowest temperature studied. This is consistent with the experimental observations that in both materials T_{FL} is as low as about 25K, and T_{FL} provides an estimation for $T_{\text{spin}}^{\text{cmp}}$ at which the spin degrees of freedom are fully screened. In summary, we clearly deduce spin-orbital separation in the completion of screening, $T_{\text{orb}}^{\text{cmp}} \gg T_{\text{spin}}^{\text{cmp}}$, for the Hund metal Sr_2RuO_4 , while this effect is less pronounced in the Mott material V_2O_3 , where χ_{orb} in addition shows a bump before it tends to saturate at lower temperatures.

In Hund metals the spin-orbital separation has been pointed out in numerical studies of the frequency dependence of the local self-energy and susceptibilities [9–11] and in an analytical estimate of the Kondo scales [13]. Here, our results reveal that it also occurs in the temperature domain. We note that our computed spin susceptibility of Sr_2RuO_4 is consistent with earlier results using a narrower temperature range [46].

Entropy. In both materials the entropy of the correlated atom reaches a plateau of $\ln(3 \times 3 = 9)$ at high temperatures as expected for a high spin ($S = 1$) state with large contribution from three active t_{2g} orbital degrees of freedom [8, 9]. Notably, in Mott systems, with decreasing temperature the plateau persists down to the temperature scale, T_{M} , until which both the spin and orbital degrees of freedom remain unquenched and the quasiparticle resonance has not yet formed in the pseudogap of the local correlated spectrum. These results are discussed in the supplement [47].

Three-band Hubbard-Hund model

Model Hamiltonian. We now turn to the 3HHM, described by the Hamiltonian

$$\hat{H} = \sum_i \left(-\mu \hat{N}_i + \hat{H}_{\text{int}}[\hat{d}_{i\nu}^\dagger] \right) + \sum_{\langle ij \rangle \nu} t \hat{d}_{i\nu}^\dagger \hat{d}_{j\nu}, \quad (1)$$

$$\hat{H}_{\text{int}}[\hat{d}_{i\nu}^\dagger] = \frac{1}{2} \left(U - \frac{3}{2}J \right) \hat{N}_i (\hat{N}_i - 1) - J \hat{\mathbf{S}}_i^2 + \frac{3}{4}J \hat{N}_i.$$

The on-site interaction term incorporates Mott and Hund physics through U and J respectively. $\hat{d}_{i\nu}^\dagger$ creates an electron on site i of flavor $\nu = (m\sigma)$, which is composed of a spin ($\sigma = \uparrow, \downarrow$) and orbital ($m = 1, 2, 3$) index. $\hat{n}_{i\nu} = \hat{d}_{i\nu}^\dagger \hat{d}_{i\nu}$ counts the electrons of flavor ν on site i . $\hat{N}_i = \sum_\nu \hat{n}_{i\nu}$ is the total number operator for site i and $\hat{\mathbf{S}}_i$ its total spin,

with components $\hat{S}_i^\alpha = \sum_{m\sigma\sigma'} \hat{d}_{im\sigma}^\dagger \frac{1}{2} \sigma_{\sigma\sigma'}^\alpha \hat{d}_{im\sigma'}$, where σ^α are Pauli matrices. We take a uniform hopping amplitude, $t = 1$, serving as energy unit in the 3HHM, and a Bethe lattice in the limit of large lattice coordination. The total width of each of the degenerate bands is $W = 4$. We choose the chemical potential μ such that the total filling per lattice site is $\langle N_i \rangle = 2$. The model is solved numerically exactly using DMFT+NRG [9, 10].

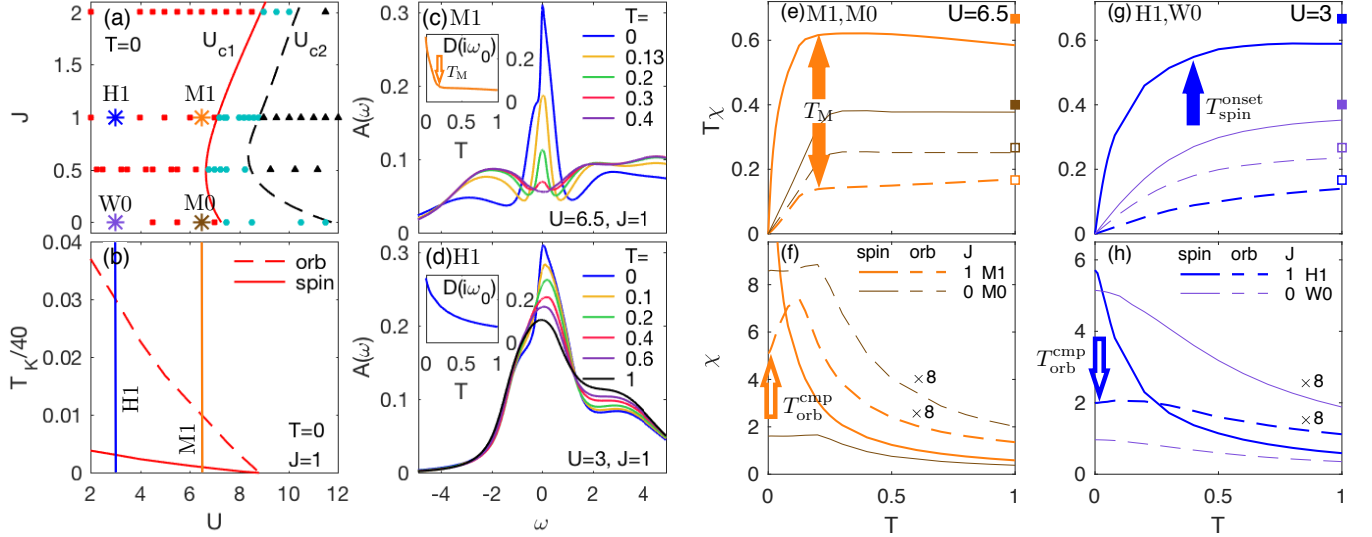


FIG. 5. Disentangling features of Mott and Hund physics in a DMFT+NRG study of the 3HHM (unit of energy: hopping amplitude $t = 1$). (a) The $T = 0$ phase diagram (cf. Fig. 5 of [10]) reveals three phases in the J - U -plane: a metallic phase (red squares), a coexistence region (blue circles), and an insulating phase (black triangles), separated by two phase transition lines U_{c1} (solid red curve), and U_{c2} (dashed black curve), respectively. In panels (c-h) we focus on four parameter combinations, indicated in (a) by colored asterisks: two Mott systems with $U = 6.5$ near the U_{c1} phase transition line, with $J = 1$ (M1) or $J = 0$ (M0); and two systems with $U = 3$ far from the transition and deep in the metallic state, a Hund system with $J = 1$ (H1) and a weakly correlated system with $J = 0$ (W0). (b) The Kondo temperatures, here shown for $J = 1$ (cf. Fig. 12 of [10]) are extracted from frequency-dependent susceptibilities at $T = 0$, as defined in [9]. T_K^{spin} (T_K^{orb}) corresponds to the screening of spin (orbital) degrees of freedom. Fermi liquid behavior sets in below the temperature scale $T_K^{\text{spin}}/40 \approx T_K^{\text{orb}}$. Orange and blue vertical lines mark the values of U used for M1 and H1, respectively. (c,d) The temperature dependence of the LDOS for M1 and H1. The energy scale of the lowest bare atomic excitations, $\pm E_{\text{atomic}} = \pm(\frac{1}{2}U - J)$, and thus the Hubbard bands, is much larger for M1 than H1. For M1 in (c) a pseudogap (a typical Mott feature) emerges when the temperature increases past a characteristic value, T_M , which lies far below the rather large scale $E_{\text{atomic}}^{\text{M1}} \simeq 2.25$. By contrast, for H1 in (d) a pronounced peak in the density of states still exists even at very high temperatures, $T > 0.5$, that exceed the rather small scale $E_{\text{atomic}}^{\text{H1}} \simeq 0.5$. The insets of (c,d) show the LDOS at the Fermi level, estimated by $D(i\omega_0) = -\frac{1}{\pi} \text{Im}G(i\omega_0)$, for M1 (orange) and H1 (blue). (f-h) The local spin and orbital susceptibilities are shown as functions of T for M1 (orange) and M0 (brown) in (e,f), and for H1 (blue) and W0 (purple) in (g,h), with $T\chi$ depicted in the upper panels (e,g) and χ in the lower panels (f,h). (e,g) For temperatures well above $T_{\text{orb}}^{\text{onset}}$ or $T_{\text{spin}}^{\text{onset}}$, respectively, $T\chi_{\text{orb}}$ and $T\chi_{\text{spin}}$ approach plateaus, indicative of a Curie law, as expected for unscreened spin or orbital degrees of freedom. The observed plateau heights are roughly comparable to the values expected [48] for free local moments with occupancy strictly equal to 2 and, for M1 and H1 (M0 and W0), spin equal to 1 (and 0), for which $T\chi_{\text{spin}}^{\text{free}} = \frac{1}{3} \langle \hat{S}^2 \rangle = 2/3$ ($2/5$) and $T\chi_{\text{orb}}^{\text{free}} = \frac{1}{8} \langle \hat{T}^2 \rangle = 1/6$ ($4/15$) indicated by filled and empty squares on the right vertical axes, respectively. (Deviations of the observed plateaus from these local moment values reflect admixtures of states with different occupancy or spin.) For M1 in (e), the Curie law ceases to hold for both χ_{orb} and χ_{spin} below about $T_M \simeq 0.2$ (orange arrow). For H1 in (g), χ_{spin} deviates from a Curie-like behavior below about $T \simeq 0.4$ (blue arrow), while χ_{orb} does not follow a Curie law in the temperature range displayed. For M0 in (e) and W0 in (g), deviations from Curie behavior set in at similar temperatures for χ_{spin} and χ_{orb} . Thus the onset of screening shows spin-orbital separation for H1, but not for M1 (due to its proximity to the Mott transition), and also not for M0 and W0 (since these have $J = 0$). (f,h) For both M1 and H1, χ_{spin} saturates at very low Fermi-liquid temperatures (not displayed here, but clearly deducible from the underlying zero-temperature NRG data [9, 10]). By contrast, χ_{orb} is approximately temperature independent below $T = 0.01$ (orange arrow) for M1 in (f) and below $T = 0.03$ (blue arrow) for H1 in (h). For M0 in (f) and W0 in (h), χ_{orb} and χ_{spin} become temperature independent at similar temperatures. Thus, the completion of screening shows tendencies of spin-orbital separation for M1 and H1 (since $J \neq 0$), but not for M0 and W0 (since $J = 0$). Moreover, $T_{\text{spin}}^{\text{cmp}}$ and hence T_{FL} is much smaller for $J \neq 0$ than for $J = 0$.

Phase diagram. The 3HHM enables the exploration of a broad region of parameters at arbitrary low temperatures. Fig. 5(a) illustrates the J - U phase diagram at $T = 0$. To illustrate the difference between large and small U , and non-zero and zero J , we will focus on four parameter combinations, denoted by M1, H1, M0 and W0, depicted by asterisks in Fig. 5(a), and defined in detail in the figure caption. The Mott system M1 ($U = 6.5$) and the Hund

system H1 ($U = 3$), both with $J = 1$, lie close to or far from the Mott transition and qualitatively mimic V_2O_3 and Sr_2RuO_4 respectively, considering their multi-orbital nature, sizable Hund's coupling and distances to the Mott transition. The Mott system M0 ($U = 6.5$) and the weakly correlated system W0 ($U = 3$), both with $J = 0$, illustrate the consequences of turning off Hund's coupling altogether.

Fig. 5 displays the LDOS, $A(\omega) = -(1/\pi)\text{Im}G(\omega)$, for M1 and H1 (c,d); the corresponding density of states at the Fermi level (insets of (c,d)), estimated by $D(i\omega_0) = -\frac{1}{\pi}\text{Im}G(i\omega_0)$; and the static local susceptibilities $T\chi$ (e,g) and $\chi \equiv \chi_d(\omega = 0)$ (f,h) for the spin (solid) and orbital (dashed) degrees of freedom of M1 (orange), M0 (brown), H1 (blue) and H0 (purple). The corresponding dynamical real-frequency spin and orbital susceptibilities are defined as $\chi_{d,\text{spin}}(\omega) = \frac{1}{3} \sum_{\alpha} \langle \hat{S}^{\alpha} \parallel \hat{S}^{\alpha} \rangle_{\omega}$ and $\chi_{d,\text{orb}}(\omega) = \frac{1}{8} \sum_a \langle \hat{T}^a \parallel \hat{T}^a \rangle_{\omega}$, respectively [48, 49], where $\hat{T}^a = \sum_{mm'\sigma} \hat{d}_{m\sigma}^{\dagger} \frac{1}{2} \tau_{mm'}^a \hat{d}_{m'\sigma}$ are the impurity orbital operators with the SU(3) Gell-Mann matrices, τ^a , normalized as $\text{Tr}[\tau^a \tau^b] = 2\delta_{ab}$. The qualitative similarities (especially of Fig. 5(c,d,g,f,h)) with those in Fig. 2 and Fig. 4 are obvious, in spite of the simplified band structure and the absence of crystal fields. Let us now discuss these in detail.

Mott system M1. The basic features of V_2O_3 are reproduced by M1, lying close to the phase transition line. At high temperatures we also observe a pseudogap in the incoherent spectra at the Fermi level, formed between two broad Hubbard sidebands, one at negative and one with minor substructure at positive frequencies, respectively (Fig. 5(c), red and purple curves). With decreasing temperature spectral weight is transferred from these high-energy humps into the pseudogap, building up a clear peak at about $T_M \simeq 0.2$, which evolves into a pronounced, sharp coherence resonance at very low temperature (Fig. 5(c), blue curve). This behavior is confirmed by $D(i\omega_0)$ (inset of Fig. 5(c)). $T\chi$ shows flat Curie behavior for both orbital and spin degrees of freedom in the pseudogapped phase at high temperatures. With decreasing temperature the orbitals and spins start to get screened simultaneously at the same energy scale, $T_{\text{orb}}^{\text{onset}} = T_{\text{spin}}^{\text{onset}} = T_M$, at which the resonance emerges in the pseudogap (Fig. 5(e)), analogously to the behavior in the Mott material V_2O_3 .

Hund system H1. For the Hund system H1 far from the phase transition line, the physical properties (LDOS, local spin- and orbital susceptibility) show the same qualitatively behavior as for Sr_2RuO_4 . At very high temperatures (above $T_{\text{spin}}^{\text{onset}} \simeq 0.4$, red, purple and black curves in Fig. 5(d)) the local spectral function has a large density of states near the Fermi energy, in contrast to the pseudogap present for M1. At these large temperatures the spin susceptibility shows Curie-like behavior, in that $T\chi_{\text{spin}}$ is essentially constant there, whereas $T\chi_{\text{orb}}$ decreases with decreasing temperature (Fig. 5(g)). This indicates that the spins are still large and (quasi-)free while the orbitals are already being screened, $T_{\text{spin}}^{\text{onset}} \ll T_{\text{orb}}^{\text{onset}}$. Below $T_{\text{spin}}^{\text{onset}}$ also the spin degrees of freedom get screened and a pronounced quasiparticle peak gradually develops, with a sharp cusp at low frequencies and very low temperatures (blue curve in Fig. 5(d)). In contrast to M1, $D(i\omega_0)$ for H1 is large already at high temperatures and increases continuously with decreasing temperature (inset of Fig. 5(d)).

Completion of screening. In principle, for both M1 and H1, i.e. both close to and far from the Mott transition, orbital screening is completed at a higher temperature than spin screening. Indeed, an approximately temperature-independent, Pauli-like susceptibility, is observed for χ_{orb} (dashed lines) below $T_{\text{orb}}^{\text{cmp}}$ (indicated by arrows in Figs. 5(f,h)), while χ_{spin} (solid lines) still increase with decreasing temperature, hence $T_{\text{orb}}^{\text{cmp}} \gg T_{\text{spin}}^{\text{cmp}}$. (This effect is more pronounced for H1, i.e. far from the Mott transition.) By contrast, the corresponding M0 and W0 curves in Figs. 5(f,h), having $J = 0$, show no spin-orbital separation for the completion of screening, i.e. $T_{\text{orb}}^{\text{cmp}} \simeq T_{\text{spin}}^{\text{cmp}}$, as described in more detail in the figure caption.

Discussion

The DMFT solution of the 3HHM with nonzero J enables us to understand the interplay between Mott and Hund physics and its materials manifestations from an impurity model perspective. Far from the transition, a picture in terms of a multi-orbital Kondo model in a broad-bandwidth metallic bath applies. Standard analysis of the logarithmic Kondo singularities showed that $T_{\text{spin}}^{\text{onset}} \ll T_{\text{orb}}^{\text{onset}}$ [13]. As we approach the Mott boundary, charge fluctuations are blocked, resulting in well-separated Hubbard bands. Here the onset of the Kondo resonance is not signaled by logarithmic singularities but instead it is driven by the DMFT-self-consistency condition [50]. In this regime the onsets of screening for spin and orbital degrees of freedom occur at the same scale, namely that where charge delocalization sets in. The spin-orbital separation in the completion of screening, which occurs at *low temperatures* in both Mott and Hund systems, can be understood from a zero-temperature analysis of the 3HHM. We define characteristic Kondo scales T_K^{orb} and T_K^{spin} , from the maximum in the zero-temperature, frequency-dependent local orbital and spin susceptibilities [9], respectively, and display them in Fig. 5(b) for $J = 1$ as a function of U . We find that $T_K^{\text{spin}} \ll T_K^{\text{orb}}$, so an intermediate region with free spins and quenched orbitals is a generic feature of multi-orbital systems with significant Hund's coupling as was surmised from earlier studies. For both the Hund and Mott system results we deduce that $T_K/40 \approx T^{\text{cmp}}$: spin-orbital separation in frequency space thus has a direct manifestation in the completion of screening as a function of temperature. Below the spin completion scale we have a Fermi liquid. As we approach the Mott boundary for increasing U the spin-orbital separation region shrinks, and all the energy scales are reduced, as shown in Fig. 5(b), elucidating the reduced $T_{\text{orb}}^{\text{cmp}}$ in the Mott system (and in V_2O_3) compared to the

Hund system (and Sr_2RuO_4).

Finally, we note that the systems M0 and W0, with $J = 0$, show no spin-orbit separation for the onset or completion of screening (see Figs. 5(e-l) and their discussion in the figure caption). Conversely, turning on J pushes the Fermi liquid scale $T_{\text{FL}} = T_{\text{spin}}^{\text{cmp}}$ strongly downward relative to $T_{\text{orb}}^{\text{onset}}$. This significantly reduces the quasiparticle weight $Z = m/m^*$ (which is proportional to T_{FL} [10]) and increases the strength of correlations. Hence the Hund system H1 is much more strongly correlated than W0, although U is the same for both. These differences leave clear fingerprints in photoemission spectra, where Z characterizes the slope of the quasiparticle dispersion. Moreover, the shape of the quasiparticle peak shows substructure indicative of spin-orbital separation for sizable J , but not for $J = 0$. For a detailed illustration of these points, see Ref. [47], Fig. S-2.

Conclusions

In conclusion, we revealed contrasting signatures of Mottness and Hundness in two archetypal materials, V_2O_3 and Sr_2RuO_4 , in the formation of the quasiparticle resonance in the local correlated spectra, and in the temperature dependence of the charge, spin, and orbital susceptibility as well as the impurity entropy. Mott and Hund physics manifest in the process in which the atomic degrees of freedom at high energies evolve towards low energies to form fermionic quasiparticles. We highlight the observation of four temperature scales that characterize the onset and the completion of screening of the spin and the orbital degrees of freedom. We find that a non-zero Hund's coupling leads to spin-orbital separation in the completion of screening at low temperatures, $T_{\text{orb}}^{\text{cmp}} \gg T_{\text{spin}}^{\text{cmp}}$, and this is more pronounced for Hund systems. However, Mott and Hund systems show contrasting behavior at intermediate to high energies, due to the very different relations of their overall quasiparticle peak width and their atomic excitation scales: $T_{\text{orb}}^{\text{onset}} \ll E_{\text{atomic}}$ for Mott systems vs. $E_{\text{atomic}} \lesssim T_{\text{orb}}^{\text{onset}}$ for Hund systems. In the Mott system V_2O_3 the strong Coulomb repulsion localizes the charge at high temperature, with decreasing temperature the onset of charge localization triggers the simultaneous onset of the screening of the spin and orbital degrees, accompanied by the formation of the coherence resonance at $T_{\text{M}} \equiv T_{\text{spin}}^{\text{onset}} = T_{\text{orb}}^{\text{onset}} \ll E_{\text{atomic}}$. In contrast, in Sr_2RuO_4 Coulomb repulsion is much weaker, so that no charge localization occurs even at very high temperatures. Therefore, charge fluctuations triggering the onset of screening are possible even at high temperatures, leading – due to the presence of sizeable Hund's coupling – to a clear separation in the energy scales at which this screening sets in for spin and orbital fluctuations, with $T_{\text{spin}}^{\text{onset}} \ll T_{\text{orb}}^{\text{onset}}$. All these findings are generic and do not depend on microscopic details. They only require a sizeable Hund's coupling, and are controlled by the distance to the Mott localization boundary. This is confirmed by a DMFT+NRG study of a model 3-band Hubbard-Hund Hamiltonian, thus establishing a general phenomenology of Mottness and Hundness in multi-orbital systems. Our results give not only new perspectives into the archetypal strongly correlated materials, V_2O_3 and Sr_2RuO_4 , but will be useful in interpreting experimental measurements on other correlated metals and in identifying the origin of their correlations.

Methods

The two prototype materials are investigated using the all-electron DMFT method as implemented in Ref. [51] based on the WIEN2k package [52] and the continuous-time quantum Monte-Carlo (CTQMC) impurity solver [53, 54]. We used projectors within a large (20eV) energy window, i.e. we used a high energy cutoff scale, to construct local orbitals, thus the oxygen orbitals hybridizing with the d orbitals were explicitly included. With such a large energy window the resulting d orbitals are very localized. In our two example materials these are the t_{2g} levels of Ru and V atoms, which we treated dynamically with DMFT, all other states were treated statically and no states were eliminated in the calculations. The nominal “double counting” scheme with the form $\Sigma_{\text{DC}} = U(n_{\text{imp}} - 1/2) - \frac{1}{2}J(n_{\text{imp}} - 1)$ was used where n_{imp} is the nominal occupancy of d orbitals. The onsite interactions in terms of Coulomb interaction U and Hund's coupling J were chosen to be $(U, J) = (6.0, 0.8)\text{eV}$ for V in V_2O_3 and $(U, J) = (4.5, 1.0)\text{eV}$ for Ru in Sr_2RuO_4 . The impurity entropy was computed by integrating the impurity internal energy up to high temperature, following Ref. [55]. Our DFT+DMFT setup was successful in describing the correlation effects in both materials [28, 31]. It captures the phase diagram of V_2O_3 which exhibits a Mott MIT and our computed electronic structure is consistent with experimental measurements [28]. The approach also describes the electronic structure of Sr_2RuO_4 and is in good agreement with the results of experimental measurements [31] and other DFT+DMFT calculations [5, 29, 30]. In addition our studies [28, 31] correctly characterize the transport and optical properties of both materials. These successes gave us confidence to extend our studies to even higher temperatures, and for quantities which have yet to be measured experimentally.

We solved the 3HHM using DMFT [19] in combination with an efficient multi-band impurity solver [9, 10], the full-density-matrix (fdm) NRG [56]. Our fdmNRG solver employs a complete basis set [57, 58], constructed from the discarded states of all NRG iterations. Spectral functions for the discretized model are given from the Lehmann representation as a sum of poles, and can be calculated accurately directly on the real axis in sum-rule conserving fashion [59] at zero or arbitrary finite temperature. Continuous spectra are obtained by broadening the discrete data with a standard log-gaussian Kernel of frequency-dependent [56, 60] width. Further, fdmNRG is implemented in the unified tensor representation of the QSpace approach [49] that allows us to exploit Abelian and non-Abelian

symmetries on a generic level [here $U(1)_{\text{charge}} \times SU(2)_{\text{spin}} \times SU(3)_{\text{orb}}$]. For further details of our DMFT+NRG calculations see the Supplementary material of [9].

Acknowledgments: Work by X.D. was supported by NSF DMR-1733071. Work by K.H. was supported by NSF DMR 1405303. Work by G.K. was supported by U.S. Department of energy, Office of Science, Basic Energy Sciences as a part of the Computational Materials Science Program. K.M.S., A.W., and J.v.D. acknowledge support from the excellence initiative NIM; A. W. was also supported by WE4819/1-1 and WE4819/2-1.

Author contributions: X.D., K.M.S. and G.K. proposed this project; X.D. performed the DFT+DMFT calculations and analyzed the results together with G.K. and K.H.; K.H. developed the DFT+DMFT code used and assisted the computation setup; K.M.S. performed the DMFT+NRG calculations; A.W. developed the NRG code and assisted K.M.S. in the initial stages of the DMFT+NRG computation. X.D. and K.M.S. drafted the manuscript with the help of G.K., K.H., A.W. and J.v.D.

Data availability: The authors declare that the data supporting the findings of this study are available within the paper [and its supplementary information files].

-
- [1] van der Marel, D. & Sawatzky, G. A. Electron-electron interaction and localization in d and f transition metals. *Physical Review B* **37**, 10674–10684 (1988).
 - [2] Imada, M., Fujimori, A. & Tokura, Y. Metal-insulator transitions. *Reviews of Modern Physics* **70**, 1039 (1998).
 - [3] Haule, K. & Kotliar, G. Coherence-incoherence crossover in the normal state of iron oxypnictides and importance of Hund’s rule coupling. *New Journal of Physics* **11**, 025021 (2009).
 - [4] Yin, Z. P., Haule, K. & Kotliar, G. Kinetic frustration and the nature of the magnetic and paramagnetic states in iron pnictides and iron chalcogenides. *Nature Materials* **10**, 932–935 (2011).
 - [5] Mravlje, J. *et al.* Coherence-incoherence crossover and the mass-renormalization puzzles in Sr_2RuO_4 . *Physical Review Letters* **106**, 096401 (2011).
 - [6] Werner, P. *et al.* Spin freezing transition and non-Fermi-liquid self-energy in a three-orbital model. *Physical Review Letters* **101**, 166405 (2008).
 - [7] de’ Medici, L. Mravlje, J., & Georges, A. Janus-Faced Influence of Hund’s Rule Coupling in Strongly Correlated Materials. *Physical Review Letters* **107**, 256401 (2011).
 - [8] Georges, A., de’Medici, L. & Mravlje, J. Strong correlations from Hund’s coupling. *Annual Review of Condensed Matter Physics* **4**, 137–178 (2013).
 - [9] Stadler, K. M., Yin, Z. P., von Delft, J., Kotliar, G. & Weichselbaum, A. Dynamical mean-field theory plus numerical renormalization-group study of spin-orbital separation in a three-band Hund metal. *Physical Review Letters* **115**, 136401 (2015).
 - [10] Stadler, K. M., Kotliar, G., Weichselbaum, A. & von Delft, J. Hundness versus Mottness in a three-band Hubbard-Hund model: on the origin of strong correlations in Hund metals. *arXiv:1808.09936 [cond-mat]* (2018).
 - [11] Yin, Z. P., Haule, K. & Kotliar, G. Fractional power-law behavior and its origin in iron-chalcogenide and ruthenate superconductors: Insights from first-principles calculations. *Physical Review B* **86**, 195141 (2012).
 - [12] Khajetoorians, A. A. *et al.* Tuning emergent magnetism in a Hund’s impurity. *Nature Nanotechnology* **10**, 958–964 (2015).
 - [13] Aron, C. & Kotliar, G. Analytic theory of Hund’s metals: A renormalization group perspective. *Physical Review B* **91**, 041110 (2015).
 - [14] Mravlje, J. & Georges, A. Thermopower and entropy: Lessons from Sr_2RuO_4 . *Physical Review Letters* **117**, 036401 (2016).
 - [15] McWhan, D. B., Rice, T. M. & Remeika, J. P. Mott transition in Cr-doped V_2O_3 . *Physical Review Letters* **23**, 1384–1387 (1969).
 - [16] McWhan, D. B., Menth, A., Remeika, J. P., Brinkman, W. F. & Rice, T. M. Metal-insulator transitions in pure and doped V_2O_3 . *Physical Review B* **7**, 1920–1931 (1973).
 - [17] McWhan, D. B. *et al.* Heat capacity of vanadium oxides at low temperature. *Physical Review B* **7**, 326–332 (1973).
 - [18] Maeno, Y. *et al.* Superconductivity in a layered perovskite without copper. *Nature* **372**, 532–534 (1994).
 - [19] Georges, A., Kotliar, G., Krauth, W. & Rozenberg, M. J. Dynamical mean-field theory of strongly correlated fermion systems and the limit of infinite dimensions. *Reviews of Modern Physics* **68**, 13 (1996).
 - [20] Kotliar, G. *et al.* Electronic structure calculations with dynamical mean-field theory. *Reviews of Modern Physics* **78**, 865–951 (2006).
 - [21] Held, K. Electronic structure calculations using dynamical mean field theory. *Advances in Physics* **56**, 829–926 (2007).
 - [22] Held, K., McMahan, A. & Scalettar, R. Cerium volume collapse: Results from the merger of dynamical mean-field theory and local density approximation. *Physical Review Letters* **87** (2001).
 - [23] Laad, M. S., Craco, L. & Müller-Hartmann, E. Orbital-selective insulator-metal transition in V_2O_3 under external pressure. *Physical Review B* **73**, 045109 (2006).
 - [24] Poteryaev, A. I. *et al.* Enhanced crystal-field splitting and orbital-selective coherence induced by strong correlations in V_2O_3 . *Physical Review B* **76**, 085127 (2007).
 - [25] Hansmann, P. *et al.* Mott-Hubbard transition in V_2O_3 revisited. *physica status solidi (b)* **250**, 1251–1264 (2013).
 - [26] Grieger, D. & Lechermann, F. Effect of Chromium doping on the correlated electronic structure of V_2O_3 . *Physical Review B* **90**, 115115 (2014).

- [27] Grieger, D. & Fabrizio, M. Low-temperature magnetic ordering and structural distortions in vanadium sesquioxide V_2O_3 . *Physical Review B* **92**, 075121 (2015).
- [28] Deng, X., Sternbach, A., Haule, K., Basov, D. N. & Kotliar, G. Shining light on transition-metal oxides: Unveiling the hidden fermi liquid. *Physical Review Letters* **113**, 246404 (2014).
- [29] Dang, H. T., Mravlje, J., Georges, A. & Millis, A. J. Band Structure and Terahertz Optical Conductivity of Transition Metal Oxides: Theory and Application to $CaRuO_3$. *Physical Review Letters* **115**, 107003 (2015).
- [30] Dang, H. T., Mravlje, J., Georges, A. & Millis, A. J. Electronic correlations, magnetism, and Hund's rule coupling in the ruthenium perovskites $SrRuO_3$ and $CaRuO_3$. *Physical Review B* **91**, 195149 (2015).
- [31] Deng, X., Haule, K. & Kotliar, G. Transport properties of metallic ruthenates: A DFT+DMFT investigation. *Physical Review Letters* **116**, 256401 (2016).
- [32] Baldassarre, L., Perucchi, A., Nicoletti, D., Toschi, A., Sangiovanni, G., Held, K., Capone, M., Ortolani, M., Malavasi, L., Marsi, M., Metcalf, P., Postorino, P. & Lupi, S. Quasiparticle evolution and pseudogap formation in V_2O_3 : An infrared spectroscopy study. *Physical Review B* **77**, 113107 (2008).
- [33] Carlo, J. P. *et al.* New magnetic phase diagram of $(Sr,Ca)_2RuO_4$. *Nature Materials* **11**, 323–328 (2012).
- [34] Hussey, N. E. *et al.* Normal-state magnetoresistance of Sr_2RuO_4 . *Physical Review B* **57**, 5505 (1998).
- [35] Yokoya, T. *et al.* Evidence for correlation effects in Sr_2RuO_4 from resonant and x-ray photoemission spectroscopy. *Physical Review B* **53**, 8151–8154 (1996).
- [36] Mo, S.-K. *et al.* Prominent quasiparticle peak in the photoemission spectrum of the metallic phase of V_2O_3 . *Physical Review Letters* **90**, 186403 (2003).
- [37] Rodolakis, F. *et al.* Quasiparticles at the mott transition in V_2O_3 : Wave vector dependence and surface attenuation. *Physical Review Letters* **102**, 066805 (2009).
- [38] Fujiwara, H. *et al.* Evidence for the constancy of U in the mott transition of V_2O_3 . *Physical Review B* **84**, 075117 (2011).
- [39] Bergemann, C., Mackenzie, A. P., Julian, S. R., Forsythe, D. & Ohmichi, E. Quasi-two-dimensional fermi liquid properties of the unconventional superconductor Sr_2RuO_4 . *Advances in Physics* **52**, 639–725 (2003).
- [40] Iwasawa, H. *et al.* High-energy anomaly in the band dispersion of the ruthenate superconductor. *Physical Review Letters* **109**, 066404 (2012).
- [41] Veenstra, C. N. *et al.* Determining the surface-to-bulk progression in the normal-state electronic structure of Sr_2RuO_4 by angle-resolved photoemission and density functional theory. *Physical Review Letters* **110**, 097004 (2013).
- [42] Mila, F. *et al.* Orbitally Degenerate Spin-1 Model for Insulating V_2O_3 . *Physical Review Letters* **85**, 1714–1717 (2000).
- [43] Park, J.-H. *et al.* Spin and orbital occupation and phase transitions in V_2O_3 . *Physical Review B* **61**, 11506–11509 (2000).
- [44] Di Matteo, S., Perkins, N. B. & Natoli, C. R. Spin-1 effective hamiltonian with three degenerate orbitals: An application to the case of V_2O_3 . *Physical Review B* **65**, 054413 (2002).
- [45] Deng, X. *et al.* How bad metals turn good: Spectroscopic signatures of resilient quasiparticles. *Physical Review Letters* **110**, 086401 (2013).
- [46] Mravlje, J. & Georges, A. Thermopower and Entropy: Lessons from Sr_2RuO_4 . *Physical Review Letters* **117**, 036401 (2016).
- [47] The impurity entropy of correlated atoms in V_2O_3 and Sr_2RuO_4 (Link to supplementary) (2018).
- [48] Hanl, M. and Weichselbaum, A. Local susceptibility and Kondo scaling in the presence of finite bandwidth. *Phys. Rev. B* **89**, 075130 (2014).
- [49] Weichselbaum, A. Non-abelian symmetries in tensor networks: A quantum symmetry space approach. *Annals of Physics* **327**, 2972–3047 (2012).
- [50] Fisher D. *et al.* Mid Gap States in The Doped Hubbard Model . *Physical Review B* **52**, 17112 (1995).
- [51] Haule, K., Yee, C.-H. & Kim, K. Dynamical mean-field theory within the full-potential methods: Electronic structure of $CeIrIn_5$, $CeCoIn_5$, and $CeRhIn_5$. *Physical Review B* **81**, 195107 (2010).
- [52] Blaha, P., Schwarz, K., Madsen, G. K. H., Kvasnicka, D. & Luitz, J. *WIEN2K, An Augmented Plane Wave + Local Orbitals Program for Calculating Crystal Properties* (Karlheinz Schwarz, Techn. Universität Wien, Austria, Wien, Austria, 2001).
- [53] Werner, P., Comanac, A., de' Medici, L., Troyer, M. & Millis, A. J. Continuous-time solver for quantum impurity models. *Physical Review Letters* **97**, 076405 (2006).
- [54] Haule, K. Quantum Monte Carlo impurity solver for cluster dynamical mean-field theory and electronic structure calculations with adjustable cluster base. *Physical Review B* **75**, 155113 (2007).
- [55] Haule, K. & Birol, T. Free energy from stationary implementation of the DFT+DMFT functional. *Physical Review Letters* **115**, 256402 (2015).
- [56] Weichselbaum, A. & von Delft, J. Sum-Rule Conserving Spectral Functions from the Numerical Renormalization Group. *Physical Review Letters* **99**, 076402 (2007).
- [57] Anders, F. B. & Schiller, A. Real-time dynamics in quantum-impurity systems: A time-dependent numerical renormalization-group approach. *Physical Review Letters* **95**, 196801 (2005).
- [58] Anders, F. B. & Schiller, A. Spin precession and real-time dynamics in the Kondo model: Time-dependent numerical renormalization-group study. *Physical Review B* **74**, 245113 (2006).
- [59] Peters, R., Pruschke, T. & Anders, F. B. Numerical renormalization group approach to Green's functions for quantum impurity models *Physical Review B* **74**, 245114 (2006).
- [60] Bulla, R., Costi, T. A. & Pruschke, T. Numerical renormalization group method for quantum impurity systems. *Reviews of Modern Physics* **80**, 395–450 (2008).